Investigation of key electronic states in layered mixed chalcogenides with a d^0 transition metal as Li-ion cathodes

Khagesh Kumar[1], Neelam Sunariwal[1], Jacques Louis[2,3], Bernhard T. Leube[2,3], Indrani Roy[1], George E. Sterbinsky[4], Jean-Marie Tarascon[2,3], Jordi Cabana[1,5]*

[1]Department of Chemistry University of Illinois at Chicago, 845 W Taylor St., Chicago, IL 60607, USA

[2]Collège de France, Chimie du Solide et de l'Énergie, UMR 8260, 11 Place Marcelin Berthelot, 75231 Paris, France

[3]Réseau Français sur le Stockage Électrochimique de l'Énergie (RS2E), 15 rue Baudelocque,

80039 Amiens, France

[4]X-ray Science Division, Advanced Photon Source, Argonne National Laboratory, 9700 S Cass Ave., Lemont, IL 60439, USA

[5]Materials Science Division, Argonne National Laboratory, 9700 S Cass Ave., Lemont, IL 60439, USA

* Corresponding Author

Abstract

Lithium-rich transition metal chalcogenides are witnessing a revival as candidates for Li-ion cathode materials, spurred by the boost in their capacities from transcending conventional redox processes based on cationic states and tapping into additional chalcogenide states. A particularly striking case is $Li_2TiS_{3-y}Se_y$, which features a d^0 metal. While the end members are expectedly inactive, substantial capacities are measured when both Se and S are present. Using X-ray absorption spectroscopy, we show that the electronic structure of $Li_2TiS_{3-y}Se_y$ is not a simple combination of the end members. We also confirm previous hypotheses that, in $Li_2TiS_{2.4}Se_{0.6}$, this behavior is underpinned by concurrent and reversible redox of only S and Se and identify key electronic states. Moreover, wavelet transforms of the extended X-ray absorption fine structure provide direct evidence of the formation of short Se-Se units upon charging. The study uncovers the underpinnings of this intriguing reactivity and highlights the richness of redox chemistry in complex solids.

1. Introduction

Lithium-ion batteries (LIBs) have revolutionized portable electronics and are playing an increasingly important role in electric vehicles and grid energy storage systems.[1–3] The exploration of high-energy-density, long-lasting, and cost-effective battery technologies has driven extensive research into novel cathode materials offering advances along key metrics,[4] following strategies such as structural and compositional design.[5,6] The latter has expanded to probe the frontiers of conventional mechanisms of electrochemical activity. Traditionally, cathodes in LIBs have relied only on reactions commonly referred to as "cationic redox"[7] involving charge compensation *via* transition metal (M) nd-Ligand np mixed states, which undergo reversible oxidation and reduction during the battery cycling. The origin of the term lies in the fact that the wavefunctions of the electrons in these hybrid states have a larger contribution from the M states than the ligands. However, this rule of design limited the achievable energy densities, as the capacity of cationic redox is inherently constrained to stable formal oxidation states of the cation.

In recent years, tapping into anion-centered states has been proposed as a promising alternative that enhances the charge capacity of the electrode and, thus, the energy density of batteries by transcending contributions only from cationic redox. Specifically, anion redox is defined as the participation of bands that have a majority contribution of the np ligand orbitals, rather than the nd cation orbitals, or even be fully non-bonding np states.[7–10] Anion redox has been invoked to explain the unconventionally high capacity of several Li-rich transition metal oxides, where characterization revealed that changes at the M center did not account for all of the activity of the material.[11,12] However, when $3d$ metals are present, as desired for application, these materials suffer from irreversible capacity loss and voltage fade due to severe structural transformations resulting from unstable electronic configurations associated precisely with the anionic redox.[13]

As an alternative, sulfides and selenides present attractive characteristics. While initially considered inviable due to their higher mass than oxides, recent work has revealed values of capacity that are so high as to render them theoretically competitive.[10,14,15] Such high capacities are critically enabled by the increased stability of holes in the anion band.[16,17] The stability explains the natural occurrence of pure sulfides (S^{2-}) and persulfides (S_2^{2-}), the latter often seen with transition metals with high d-counts owing to the interaction between their lower-lying d-orbitals and the S sp band.[18] For Ti, both disulfide (TiS_2) and trisulfide (TiS_3) exist, containing only S^{2-}, and a combination of S^{2-} and S_2^{2-} respectively.[19,20] The stability of two different electronic (2- vs. 1-) and geometric (isolated S centers vs. S-S bonds) states of S with Ti suggest that anionic redox should be facile with $Ti^{4+}(d^0)$. In this context, studies of Li_2TiS_3 were pursued owing to its high theoretical capacity of 339 mAh/g, but it was found to be essentially inactive toward Li de-intercalation.[14] The addition of $d^{n>0}$ cations (Ti^{3+}, Fe^{2+}, Co^{2+}) were subsequently explored, where conventional mechanisms of cationic activity were insufficient to account for the high capacities observed.[14,15,21] Interestingly, more recently, substitution with Se^{2-} was also revealed as an effective strategy to activate Li_2TiS_3 by adjusting the energy and symmetry of the p states without adding d electrons.[22] In particular, Se^{2-} was chosen because it has donor p levels at higher energy than S, which can hypothetically provide additional stability to holes, and a bigger ionic radius, which leads to local symmetry changes when the two anions coexist around a transition metal center. The substitution of Se^{2-} resulted in compounds that exhibited a bell-shaped curve in the number of Li-ions extracted during cycling, with $Li_2TiS_{2.4}Se_{0.6}$ showing the highest gravimetric capacity. However, little is known about the underlying electronic phenomena responsible for this electrochemical activation and the specific states contributing to the electrochemical capacity of the $Li_2TiS_{2.4}Se_{0.6}$. A mechanistic understanding of these states will help build a framework for electrochemical activation procedures, hence enabling continued development of high-capacity cathode materials based on such environmentally friendly elements.

In this work, we focus on unraveling underlying electronic and structural evolution in $Li_2TiS_{3-y}Se_y$ (y = 0, 0.6, 1.5, 0.5, and 3) using ligand and metal X-ray absorption spectroscopy (XAS) and extended x-ray absorption fine structure (EXAFS). XAS and EXAFS provide valuable insights into the redox compensation and the corresponding local structural changes. Information from the electronic structure of the metal and ligands revealed insight into the trends in electrochemical activity with the amount of Se^{2-} substituted.[22] The reversible electrochemical activity $Li_2TiS_{2.4}Se_{0.6}$ is also studied to understand the underlying mechanism of redox compensation. This work presents spectroscopic evidence of the formation of both S_2^{n-} and Se_2^{2-} from oxidation during the charging process. Particularly, we present clear structural evidence of the formation of Se-Se bonding distances associated with persulfide units.[23,24]

2. Results and Discussion

2.1. Structural characterization of $Li_2TiS_{3-y}Se_y$

$Li_2TiS_{3-y}Se_y$ with y = 0, 0.6, 1.5, 2.5, and 3 were synthesized using a solid-state method, as reported in Leube *et al.*[22] A powder X-ray diffraction(XRD) pattern was collected for the as-synthesized material, as shown in Figure S1 a). The pattern reveals a highly crystalline material, and the peaks can be indexed to the rhombohedral R-3m space group; no impurities were identified. The pattern was then refined to extract lattice parameters; the extracted lattice parameters are presented in Figure S1 b). The *a* and *c* lattice parameters show a linear increase with the increase in Se content following Vegard's law.

2.2. XAS of pristine $Li_2TiS_{3-y}Se_y$

The chemical states were investigated using X-ray absorption spectroscopy (XAS) collected at the Ti $L_{2,3}$-, Ti K-, S K-, and Se K-edges (see **Figure** 1). The Ti $L_{2,3}$-edge XAS reflects the transition of an electron from $2p^{1/2}$ and $2p^{3/2}$ to $3d$ states resulting in L_3 (458 to 462 eV) and L_2 (462 -468 eV) manifolds, respectively. The lineshape of the Ti $L_{2,3}$-edge spectra is very sensitive to coordination and oxidation state.[25] The Ti K-edge whiteline (~4975 eV) comprises an electronic dipole transition from $1s$ to $4p$ states and subsequent photoionization, with a pre-edge (~4969 eV) resulting from a dipole-forbidden transition to Ti $3d$-ligand np states.[26] The Ti $L_{2,3}$-edge shape aligns well with the reported spectra for Ti^{4+} in an octahedral environment,[27,28] so the two strong peaks in the L_2 and L_3 regions were assigned to t_{2g} and e_g states (See **Figure** 1 a),[25] with the additional signals arising from the effects of the multiplet splitting.[29,30] Li_2TiS_3 exhibits a pronounced feature around 457 eV, which reflects a forbidden transition in spin-orbit coupling,[31] but becomes allowed because of the splitting of the multiplet in the presence of multiple pd interactions due to covalency.[30,32–35] The feature intensity lowered significantly with increased Se^{2-} substitution.[32] The intensity of the feature suggests are notable distortion of the Ti^{4+} octahedral environment in this compound. Since the main peaks at the Ti L_3-edge is sensitive to symmetry changes,[28] the subtle variation for compositions from y = 3 to 0.6 can be attributed to more subtle and monotonic structural distortions of the Ti^{4+} octahedral environments. Likewise, the position of the Ti K-edge whiteline in all materials matched the spectra of TiS_2, indicating a formal oxidation state of Ti^{4+},[27,36,37] consistent with the observations at the $L_{2,3}$-edge (See **Figure** 1 b). The pre-edge intensity at ~4875 eV is a good measure of the Ti coordination number.[26] It matches with Ti in a sixfold coordination environment. Changes in the pre-edge shape, whiteline peak at ~4975 eV, and subsequent fine structure also indicate changes in the local structural arrangement, which are most visible for Li_2TiS_3, consistent with observations at the Ti $L_{2,3}$-edge.

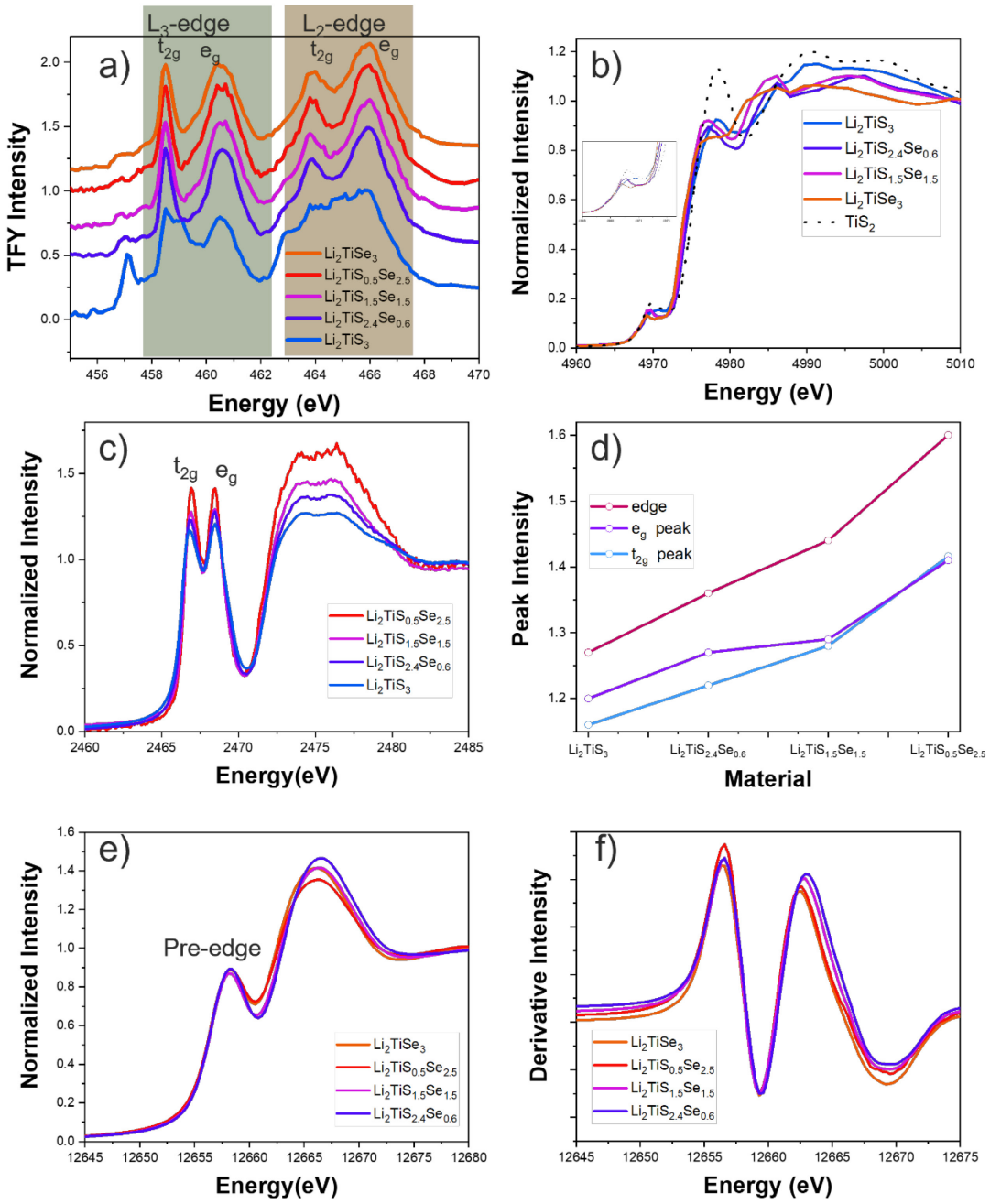

Figure 1. XANES spectra for pristine $Li_2TiS_{3-y}Se_y$ for y = 0, 0.6, 1.5, 0.5, and 3 collected at a) Ti $L_{2,3}$- b) Ti K-, c) S K- and e) Se K-edges. d) Intensity of t_{2g} and e_g pre-edge peaks and edge peak in the S K- XANES and f) first derivative plot of Se K-XANES. Inset in b) shows the zoomed-in at the Ti K-pre-edge.

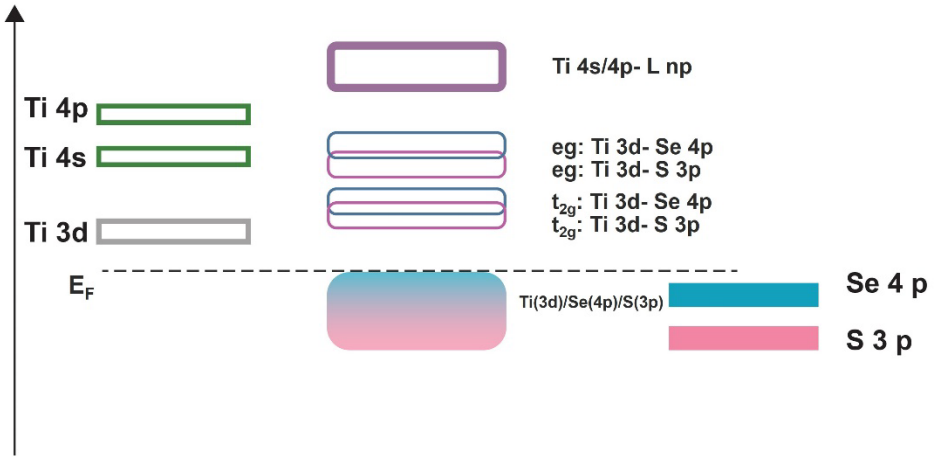

Figure 2. Schematic representation of bands in $Li_2TiS_{3-y}Se_y$ as predicted from Fukui functions[22] due to locally distorted $TiCh_6$

The S K- and Se K-edge X-ray absorption near edge structure (XANES) can be divided into two regions of interest: pre-edge and main edge. The pre-edge region is below 2472 eV and 12662 eV for S K- and Se K-edge, respectively, whereas the edge encompasses a region higher in energy than the pre-edge (**Figure 1** c, e).[23] The pre-edge results from a dipole allowed the transition of an electron from S/Se 1s to ligand np-Ti 3d (n =3 and 4 for S and Se, respectively). The main edge results from the S/Se 1s transitions to ligand np−Ti 4s/4p hybridized orbitals, followed by higher transitions and photoionization.[23]

The S K-XANES of $Li_2TiS_{3-y}Se_y$ shows two peaks in the pre-edge across the composition, reminiscent of the spectrum of S K-XANES of TiS_2.[36,38] Thus, we assign them to the unoccupied S 3p-Ti3d t_{2g} and e_g states in an octahedral field of S around Ti. The splitting of these states, ~2 eV, was similar to the crystal field splitting computed by density functional theory (DFT) by Leube *et al.*[22] The increase in Se^{2-} substitution leads to an increase in the pre-edge and edge intensity (**Figure** 1 c), but their shape and position remain constant. The latter two features mean that there was no change to the energy and symmetry of the S 3p-Ti 3d hybridized bands. To understand the changes, it is instructive to look at a simplified band structure schematic (see **Figure** 2).[10,23] In the absence of a change in the overall band structure, the intensity of these pre-edge peaks depends on the formal oxidation state of the compound and the contribution of S states to the S 3p-Ti 3d hybridized bands. The fact that these compounds are d^0, as indicated by Ti XAS, and the fixed S K-edge position rules out the possibility of oxidation state changes. Instead, we hypothesize that the increase in pre-edge intensity stems from the increased overlap between S 3p and Ti 3d states due to the substitution of the larger Se anion, possibly by distorting the octahedron in a way that enhances directional overlap and/or pushes the Ti and S ions closer to each other.[39] The increased overlap due to the local distortion could be indicative of a change in electronic structure so that there is a greater anion character in the occupied states close to the Fermi level.

To obtain a full picture, Se K XANES analysis was conducted on $Li_2TiS_{3-y}Se_y$ with y = 0.6, 1.5, 2.5, and 3 (**Figure** 1 e). The pre-edge region displays a singular broad feature, despite the existence of a crystal field, due to the considerably shorter 1s core-hole lifetime at the Se K-edge.[40] Its position and intensity were constant with Se substitution, suggesting no significant change to Ti-Se hybridized states. However, as the

Se content increased, a small red shift in the edge position was observed, which is clearly seen as a shift of the corresponding peak in the first derivative in the spectrum, **Figure** 1 e.

Computed Fukui functions provided by Leube *et al*.,[22] suggest that hybridized Ti($3d$)/Se($4p$)/S($3p$) states are introduced near the Fermi level in mixed S/Se compounds as opposed to the existence of only S/Se nonbonding np levels in the presence of only one anion (**Figure** 2).[22] We posit that this phenomenon could be viewed as enhancing the charge transfer between the anions and Ti. In the case of S, it would seem to be reflected as an enhancement of S character in the unoccupied d states, whereas the shift of the Se K-edge could be the reflection of the enhanced charge transfer being primarily imposed to the heavier chalcogenide.

To explore whether these subtle electronic structure changes are associated with local structural changes around the Se center, we employed extended X-ray absorption fine structure (EXAFS). The Fourier-transform magnitude with a k-weight of 2 is presented in **Figure** 3 a, revealing a prominent peak at approximately 2 Å and a second peak set at around 3-3.5 Å. The first peak corresponds to the Se-Ti bonding path, while the second peak in Li_2TiSe_3 is assigned to the Se-Se/S bonding path, as depicted in **Figure** 3 c. As the Se content decreases from y=3 to 0.6, there is a progression of the Se-Se/S path from ~3.3 to 2.9 Å, which we associate with compression of the Se-Se/S bonding path when a smaller scattering path develops as the smaller S anion is introduced, consistent a linear decrease in the lattice parameters of the unit cell.[22] This compression could be associated with an enhanced charge transfer from anions, especially Se, to Ti. The changes can also be seen in the scattering function in k-space (Figure S2), with a shift to a higher k with an increase in S content along with peak intense changes around 4.2 $Å^{-1}$ and 6.5 $Å^{-1}$. Intermediate values of y showed very weak features at these distances, which are tentatively ascribed to atomic disorder, such as stacking faults, which were also observed in powder diffraction data.[22] Attempts to fit the data were not successful. Fits with the simple disordered structure from diffraction were unsatisfactory, likely due to the existence of local ordering in the otherwise disordered lattice. Further analysis of this point could not be performed due to the correspondingly high number of unknown parameters that would be needed, compared to possible parameter that could be extracted from the data.

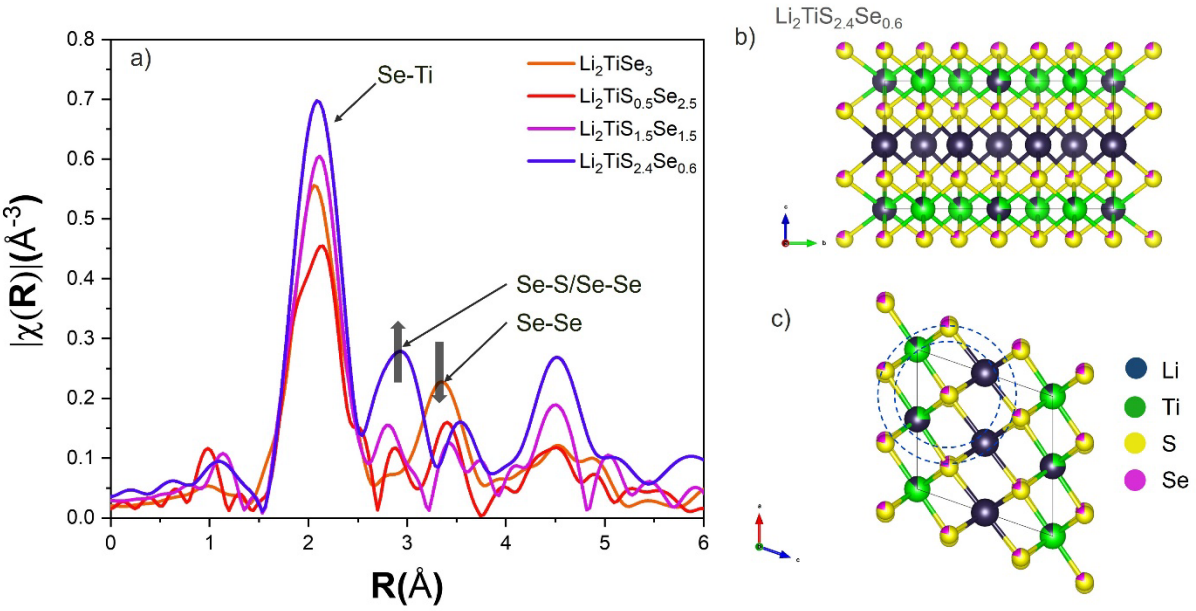

Figure 3. a) Fourier transform magnitude of the Se K-edge oscillations for $Li_2TiS_{3-y}Se_y$ with y = 0.6, 1.5, 0.5 and 3. Graphical representation of the structure of $Li_2TiS_{2.4}Se_{0.6}$ along b) *a* axis and c) *b* axis. The dotted circles in c) illustrate Se-Ti and Se-S/Se-Se paths in the EXAFS

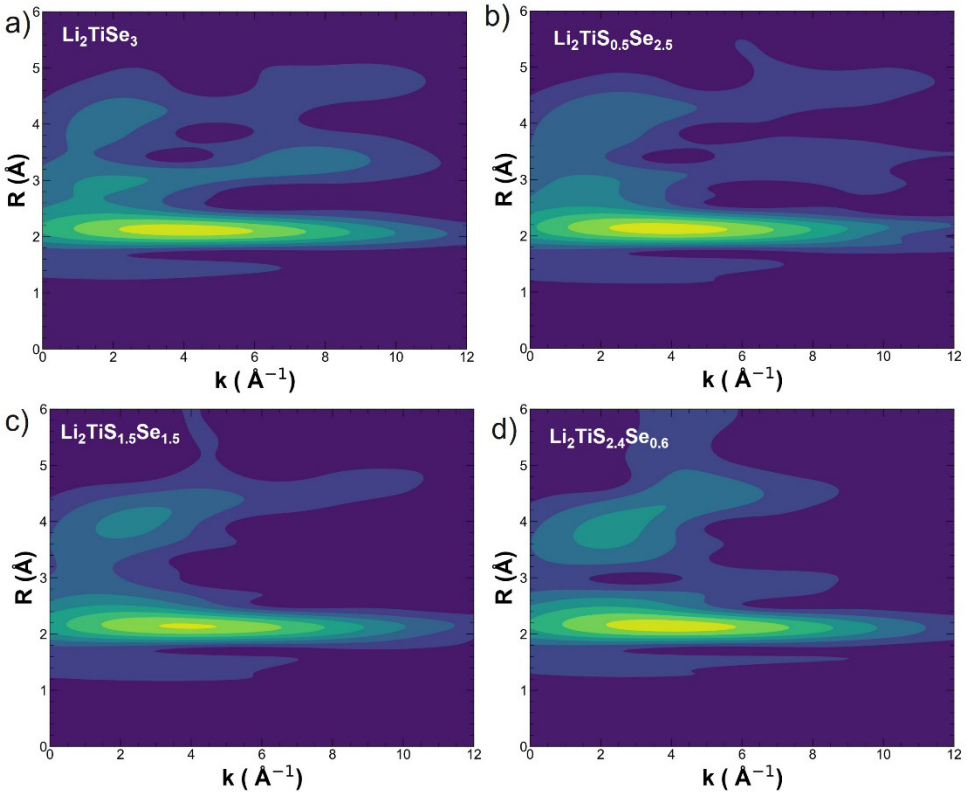

Figure 4. Wavelet transform at Se K-edge for a) Li_2TiSe_3, b) $Li_2TiS_{0.5}Se_{2.5}$, c) $Li_2TiS_{1.5}Se_{1.5}$, and d) $Li_2TiS_{2.4}Se_{0.6}$

In order to better differentiate the contributions of each atom to the atomic paths, we analyzed the wavelet transform (WT)-EXAFS of the experimental χ(k), using a Cauchy mother wavelet.[41] The WT generates a 2D plot of the Fourier pair k and R (**Figure** 4), facilitating a more precise analysis of the contributing scatterers in a path. Signals associated with an element with higher Z (e.g., Se vs Ti/S), and, thus, high scattering factor, appear at higher k value in WT.[41] The first shell at approximately 2 Å exhibits a contribution from a feature centered at around 4 $Å^{-1}$, confirming a Se-Ti scattering path. No other high Z scattering feature was observed in the first shell. Contributions centered at ~8 $Å^{-1}$, associated with Se-Se paths, were visible at approximately 3.3 Å for y = 3. However, they became less prominent as y decreased because of the replacement of Se by S in the second coordination shell of Se.

2.3. XAS of electrochemically cycled $Li_2TiS_{2.4}Se_{0.6}$

The electrochemical activity of $Li_2TiS_{3-y}Se_y$ (with y = 0.6, 1.5, 2.5, and 3) showed a bell-shaped curve with y.[22] The gravimetric discharge capacity peaked at 235 mAh/g for y = 0.6 (**Figure** 5).[22] The first charging process consists of a voltage plateau at 2.7 V vs. Li^+/Li^0. Upon discharge, all the extracted Li can be re-intercalated into the materials through a slightly more sloping, S-shaped profile centered at 2.4 V vs. Li^+/Li^0, in agreement with reports in the literature for this compound.[14,15] 1.6 equivalent of Li can be reversibly cycled in the $Li_2TiS_{2.4}Se_{0.6}$. Samples of $Li_xTiS_{2.4}Se_{0.6}$ were harvested after being charged to 1.4 Li, 0.8 Li, and 3 V and discharged to 1 Li and 1.7 Li, as indicated in **Figure** 5, to perform *ex-situ* XAS measurements. The samples are labeled according to **Figure** 5.

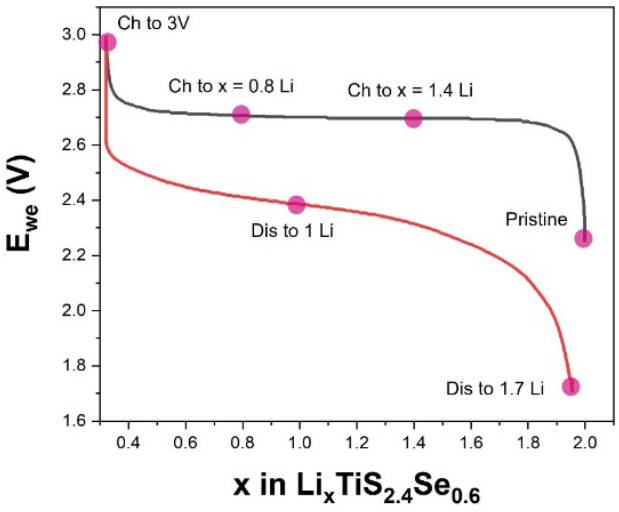

Figure 5. Galvanostatic charge and discharge curves of $Li_2TiS_{2.4}Se_{0.6}$ against Li^+/Li in the voltage range 1.7–3 V at a rate of C/10. The state of charge at which samples were studied is marked i.e. pristine, charged to x= 1.4 Li, to x = 0.8 Li, to 3V, and discharged to 1 Li and 1.7 Li.

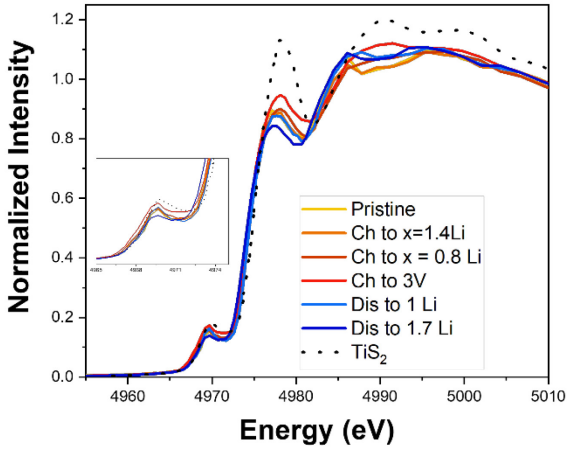

Figure 6. Ti K-edge XANES spectra of $Li_2TiS_{2.4}Se_{0.6}$ in the pristine state and when charged to x= 1.4 Li, to x = 0.8 Li, to 3V, and discharged to 1 Li and 1.7 Li. Inset shows the zoomed-in at the Ti K-pre-edge

Figure 6 presents the Ti K-XANES spectra of the cycled samples. In the pristine state, Ti exhibited a +4 oxidation state and an octahedral symmetry, as previously discussed. The whiteline position remained unchanged upon charging and matched with the position of TiS_2, indicating that Ti maintained its +4 oxidation state. However, the whiteline and pre-edge intensity increased slightly, suggesting changes in the local structure. Upon discharge, the edge position also remained unchanged, indicating the persistence of the +4 oxidation state, and the whiteline and pre-edge intensity returned to a state resembling the pristine sample. However, deviations in the pre-edge intensity and the edge position indicate subtle changes in the local coordination environment after one cycle.[42] Overall, the pre-edge intensity at all states in the cycle reflects Ti in an octahedral coordination.[26] Leube *et al.* reported a slight reduction to Ti^{3+} upon discharge based on Hard X-ray Photoelectron Spectroscopy (HAXPES) data collected at 10 keV,[22] which is not obvious from our data. We attribute the apparent discrepancy to a disparity in probe depth, as Ti HAXPES probes approximately 40 nm into the sample and, thus, is dominated by surface species, whereas Ti K XANES has a much larger probe depth of 5 μm and, thus, is dominated by the bulk of the material.[22,43] This observation suggests that, at the ensemble average, Ti is not undergoing redox.

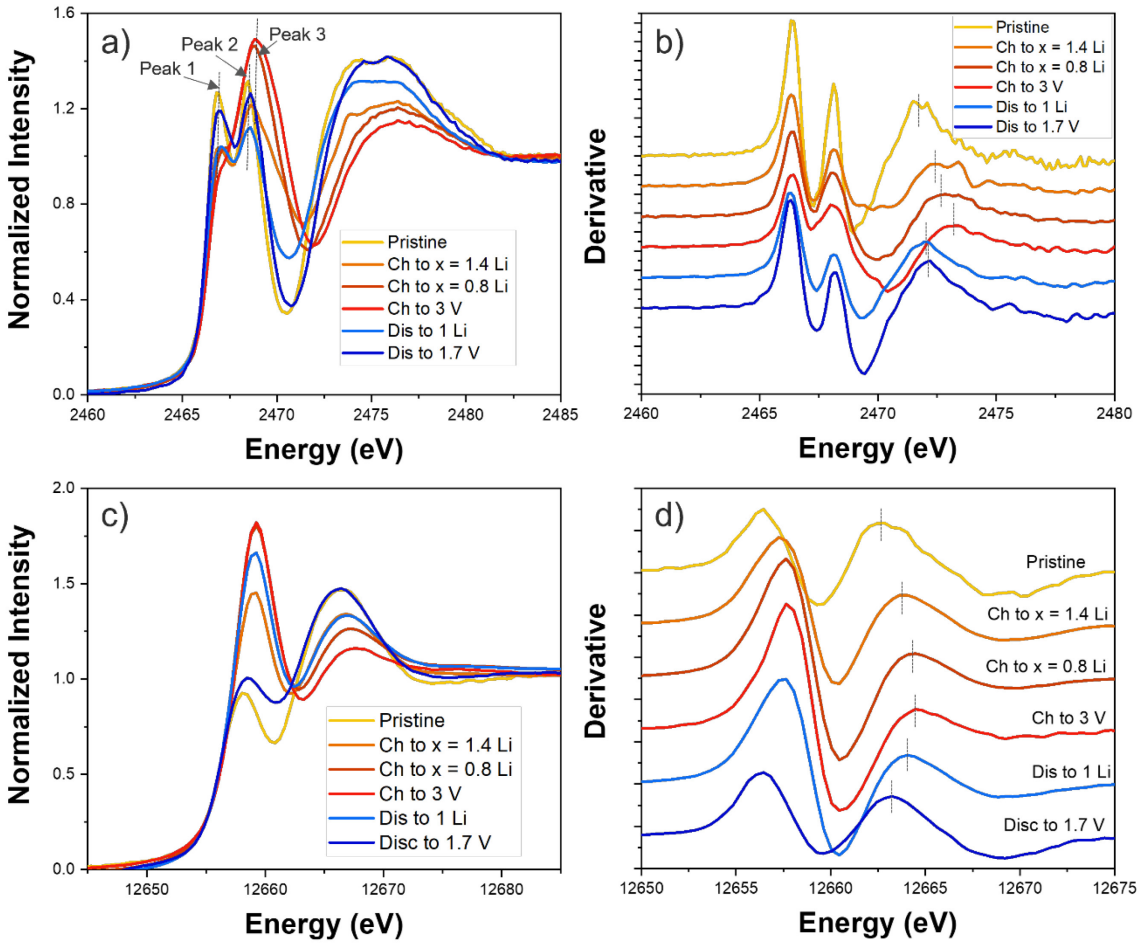

Figure 7. XANES spectra of $Li_2TiS_{2.4}Se_{0.6}$ in the pristine state and when charged to x= 1.4 Li, to x = 0.8 Li, to 3V, and discharged to 1 Li and 1.7 Li at a)S K-edge, b) first derivative of a) and at c) Se K-edge d) first derivative of c). The S K- and Se K-edge positions are marked with dash lines in b) and d).

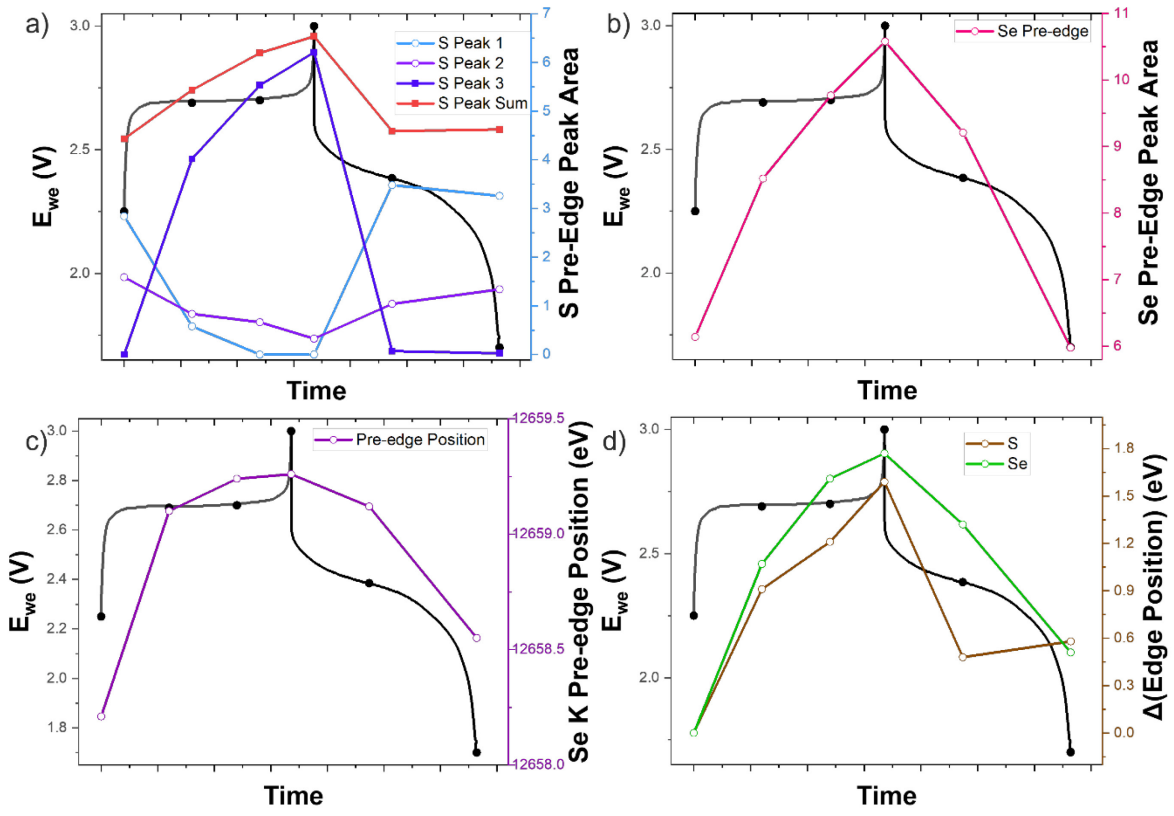

Figure 8. $Li_2TiS_{2.4}Se_{0.6}$ XANES analysis at S K- and Se K-edge for pristine, and samples charged to x= 1.4 Li, x = 0.8 Li, to 3V, and discharged to 1 Li and 1.7 Li. a) S K- pre-edge area calculated by fitting t_{2g} and e_g features and the new feature appearing upon oxidation as peak 1, peak 2, and peak 3, respectively with pseudo-Voigt functions, and Peak sum represents the sum of Peak 1, 2, and 3, b) Se K- pre-edge area, c) Se K-pre-edge position and d) Change(Δ) in S K-and Se K-edge positions overlaid on the galvanostatic charge and discharge curves for $Li_2TiS_{2.4}Se_{0.6}$.

S K- and Se K-edge were measured to evaluate redox at the anionic centers. Upon charging, the total intensity of the S K pre-edge increases, and its center of gravity blueshifts, concurrent with a move of the absorption edge to higher energy (**Figure** 7 a, b, and **Figure** 8 a, d) that is ascribed to an increase in the Z_{eff} of S. When charged to 1.4 Li and 0.8 Li, the pre-edge shows a lowering of the intensity of the t_{2g} feature, simultaneous to the growth of a very prominent signal at ~2469 eV, higher than the original e_g feature. Upon charging to 3V, the t_{2g} feature remains as a small shoulder along with a slight shift and increased intensity of the new signal. These changes at the pre-edge are different from a conventional intercalation sulfide such as TiS_2,[27,37] in which the intensity change in S K-pre-edge reflects cationic redox through hybridization, and the changes consist of modulation of the pre-edge intensity with no change in position. The pre-edge changes resemble the recent study of anion redox in Li_2FeS_2 by See *et al.*,[44] in which charging leads to the formation of a new peak in the pre-edge corresponding to oxidized S^{2-}. To further explore the origin of these changes, we compared the evolution of the spectra to TiS_2 and TiS_3. Whereas both present Ti in a formal oxidation state of 4+, only octahedra formed by isolated S^{2-} units were observed in the TiS_2, whereas the 6-coordinated Ti cation is surrounded by both S^{2-} and S_2^{2-} species in TiS_3, as demonstrated by the existence of short S-S distances.[20,45] The S K-edge spectrum of TiS_3 displays a single, broad pre-edge

peak at slightly higher energy than the t_{2g}-e_g doublet of TiS_2.[20] The spectral differences between TiS_2 and TiS_3 match very well with the evolution of $Li_2TiS_{2.4}Se_{0.6}$ upon de-intercalation of Li, suggesting that the Ti-S bonding shifts between only involving S^{2-} to the presence of both S^{2-} and an oxidized unit, possibly S_2^{n-} ($2 \leq n$), while the formal oxidation state of Ti remained constant. The evolution in the Se K-edge XANES during charging is similar (**Figure** 7 c and d). The movement of the edge to higher energy indicates an increase in the Z_{eff} of Se centers, whereas the increase in pre-edge intensity and blueshift indicates a change in the Se-Ti hybridized states. Given that the Ti states did not change, according to XAS, we assign these changes to redox compensation at the Se centers, just like S.

To gain more quantitative insight into the evolution of the material, the pre-edge and edge signals of S were fitted with 2-3 pseudo-Voigt and Gaussian functions, respectively, as shown in **Figure** S3,[40,46] and the pre-edge peak of Se was fitted using a pseudo-Voigt function as shown in **Figure** S4. The area under the curve of the respective fitted peak in the pre-edge was extracted to track its evolution. The peak position was determined using the inflection point of the corresponding signal. The trends of the area under these peaks are displayed in **Figures** 8a and b, whereas the Se pre-edge position is shown in **Figure** 8c. Lastly, the change in position (ΔEdge position) of the absorption edge for both S and Se was defined as the difference in the first moment of each sample relative to the pristine state (**Figure** 8d). The trends in area and position presented in **Figure** 8 are plotted against the galvanostatic charge and discharge curve.

The S K-edge XAS peaks at the energy of the t_{2g} and e_g features in the original environment (peak 1 and 2 in **Figure** 8a) gave way to peak assigned to oxidized S species (peak 3). The overall trend was for the total intensity at the pre-edge to increase linearly with charging, concurrent with a similar response of the edge position. Similar linear trends were observed in the intensity and position of the Se pre-edge and the position of its absorption edge (**Figures** 8b, c, d). These observations reveal that both Se and S centers participated at all states during the charge. The increases in pre-edge area and shift in edge position are both consistent with the mixed Ti 3*d*-Se 4*p*-S 3*p* character of the states available for delithiation, according to the Fukui functions computed by Leube *et al.*[22] However, the total pre-edge area increase when charged from pristine to 3V (fully charged) at S K-edge was ~1.5 times from 4.5 units to 7 units (**Figure** 8 a), whereas at the Se K-edge was 1.75 times from ~6 units to 10.5 units. Furthermore, the overall change in edge position was also somewhat more pronounced for Se than S. Both suggest that Se states contribute more to the capacity of the material (**Figure** 8 b), despite the noticeably smaller content of Se than S in the compound. The overall linear trends and the more pronounced changes for Se are in excellent agreement with conclusions from Leube *et al.* based on trends of HAXPES and Bader charge analyses.[22]

During discharge, the processes were reversed. However, the change was non-linear at the S K-edge. The overall pre-edge intensity and the position of the absorption edge already resembled the pristine spectrum when going from $Li_{0.4}TiS_{2.4}Se_{0.6}$ to $Li_1TiS_{2.4}Se_{0.6}$ (**Figure** 8 a and d), indicating the activity of S is more prominent in the initial than latter stages of discharge. The spectrum of the fully discharged electrode did not perfectly match the pristine state, with a slightly lower pre-edge intensity and a higher edge position. Considering the very high reversibility of the electrochemical capacity in **Figure** 5, this behavior points to hysteresis in the chemical pathway in the forward and backward reactions that may be related to the differences in the electrochemical profile between charge and discharge. The irreversible structural changes during the first charging, especially in the interlayer Ti/Li ordering, were reported by Leube *et al.*[22] could also be related to this behavior. In contrast, the trends at the Se K-edge were linear upon discharge, with a reversal to the pristine spectrum only after the full discharge, rendering the evolution during cycling more symmetric at the Se center compared to S. Nonetheless, the reversal was not complete, possibly due to some remaining oxidized Se^{n-}.

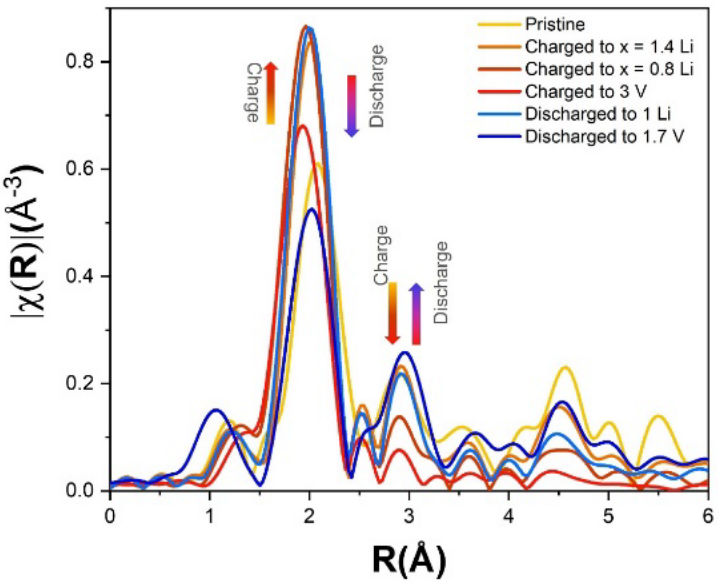

Figure 9. Se K- Fourier transform magnitude (k^2 weighted) EXAFS spectra of $Li_2TiS_{2.4}Se_{0.6}$ in the pristine state, when charged to x= 1.4 Li, when charged to x = 0.8 Li, when charged to 3V, when discharged to 1 Li, when discharged to 1.7 Li.

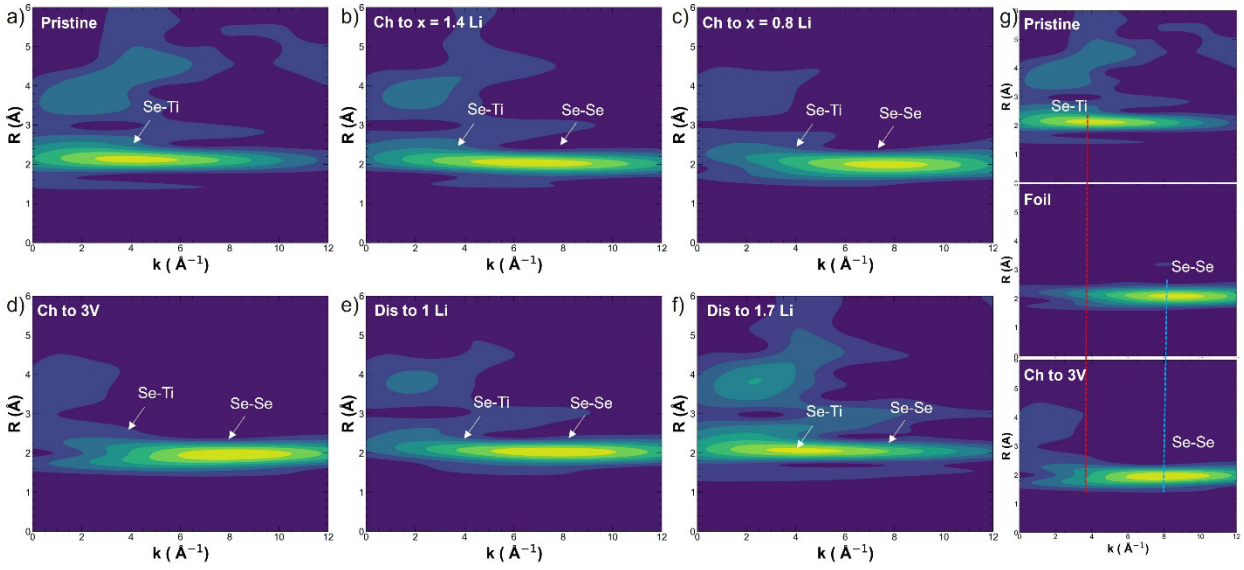

Figure 10. Se K-Wavelet transform EXAFS of $Li_2TiS_{2.4}Se_{0.6}$. a) in the pristine state, b) when charged to x= 1.4 Li, c) when charged to x = 0.8 Li, d) when charged to 3V, e) when discharged to 1 Li, f) when discharged to 1.7 Li and g) comparison of pristine and Ch to 3V with Se foil.

To further explore the nature of the electron depletion at the Se centers, EXAFS analysis was performed for the cycled samples (**Figure** 9). Upon charging, the intensity of the Se-Ti path, around ~2 Å, increases, suggesting an increase in the number of scatterers in the shell. Conversely, the peak intensity of the second feature decreases. These trends are largely reversed upon discharge. Changes to the EXAFS spectra were seen in k-space in **Figure** S5 with low-k features lowering in intensity upon charging, and the intensity recovers upon discharge. To resolve the scattering elements in R-space, WT-EXAFS (**Figure** 10) was carried out for the pristine and cycled samples. WT-EXAFS revealed that the first shell moves toward a higher k, from its center of gravity being at ~4 $Å^{-1}$ to 8 $Å^{-1}$, as the material is charged (**Figure** 10 a-d). Comparison with the first shell of Se foil (**Figure** 10 g), which has only Se-Se paths, gives evidence of the onset of short Se-Se paths upon oxidation (**Figure** 10 c), which dominate the signals at this distance because of the stronger scattering factor compared to Se-Ti interactions.

Sample	**Path**	**E_0(eV)**	**CN**	**R (Å)**	**σ^2 ($Å^2$)**	**R-factor**
Pristine	Se-Ti	7.07	1.94(1.04)	2.55(0.05)	0.01(0.008)	0.07
Ch to 1.4 Li	Se-Se	8.17	0.97(0.59)	2.37(0.04)	0.003*	0.042
	Se-Ti		0.98(0.37)	2.59(0.10)	0.003*	
Ch to 0.8 Li	Se-Se	3.90	1.20(0.23)	2.34(0.05)	0.003*	0.019
	Se-Ti		0.75(0.24)	2.59(0.02)	0.003*	
Ch to 3V	Se-Se	-1.34	1.74(0.51)	2.33(0.02)	0.007(0.001)^	0.002
	Se-Ti		0.28(0.27)	2.54(0.11)	0.007(0.001)^	
Dis to 1 Li	Se-Se	6.44	0.78(1.27)	2.34(0.06)	0.001(0.008)^	0.029
	Se-Ti		0.69(0.23)	2.56(0.11)	0.001(0.008)^	
Dis to 1.7 Li	Se-Ti	4.10	1.05(0.52)	2.48(0.04)	0.005(0.05)	0.11

Table 1. EXAFS fitting parameters of $Li_2TiS_{2.4}Se_{0.6}$ for the pristine and cycled samples. R is the apparent distance in Å from the central atom to the scatterer, k is the scattered photoelectron wave vector, CN is the number of scatterers, σ^2 is the Debye−Waller factor, and R-factor is the goodness of fit. * indicates fixing the σ^2 value for both shells to 0.003, and ^ denotes using the same σ^2 for both the Se-Ti and Se-Se paths; the σ^2 values were fixed to lower the number of unknown variables for the fitting and improve the statistics. Fourier-transform range: $2.7 \leq k(Å^{-1}) \leq 12$ and fitting range: $1.1 \leq R\ (Å) \leq 2.4$. The corresponding EXAFS fits are in shown in **Figure** S6 and S7.

To quantitatively analyze these changes, the first shell of all EXAFS spectra was fitted with Se-Ti and Se-Se paths, and the fitting parameters are presented in **Table** 1, with the fitting results shown in **Figure** S6 and S7. In the pristine sample, only the Se-Ti path could be fitted satisfactorily. Despite multiple attempts, fits including the shells beyond the first with a simple structure yielded deficient R-factors, suggesting the existence of structural disorder and, thus, a higher number of unknown parameters for the possible paths than could be reliably fit with the data. Upon charging to x =1.4 Li, the short Se-Se path becomes apparent and can be fitted. With further charging, the coordination number (CN) of the new shorter Se-Se path

increased and, as could be expected from the XANES analysis, peaked at 3 V, indicating more Se-Se species. The CN determined from EXAFS denotes an average number of shorter Se-Se paths around the Se center in the first shell. A value lower than the crystallographic coordination number signifies the increase in other anionic distances in the coordination sphere of Se as a result of short Se-Se interactions, and, possibly, that the domains with shorter Se-Se bonds are small, similar to the what occurs in small metal nanoparticles due to averaging even when they possess the same crystal structure as bulk.[47,48] The fact that the Se-Se path length extracted from EXAFS fits (**Table** 1) is comparable to elemental Se indicates that the distance is sufficiently close to induce orbital overlap and, thus, bonding through formation of Se_2^{2-} units in the material as Se undergoes charge compensation.[17] The values are also in close agreement with $(Se_2)^{2-}$ bond lengths reported in the literature.[49–51] If we assume a random arrangement of Se and S in the $TiCh_6$ (Ch=S, Se) octahedra that form the structure of $Li_2TiS_{2.4}Se_{0.6}$, consistent with the diffraction analysis by Leube *et al.*,[22] the probability of at least two Se being located next to each other (needed for Se-Se bond formation) in the octahedra with the distribution of S and Se is calculated to be about 29.5% (see **Table** S1), plausibly enough to detect Se-Se units by EXAFS.

Upon discharge, the center of gravity of the first shell shifts back to lower k in the WT-EXAFS, as the Se-Se distance returns to isolated Se^{2-} units. The fully discharged sample is not exactly the same as pristine and shows some intensity at high k in the first shell (see **Figure** 10 f), indicating a small presence of remaining oxidized Se. Concurrently, the CN of the Se-Ti path decreased during discharge. The trends in the CN of Se-Ti and the short Se-Se path explain the observation of the intensity changes seen in **Figure** 10.

3. Conclusion

In this study, we revealed the nuanced variations in the local electronic and geometric structure of $Li_2TiS_{3-y}Se_y$ with y = 0, 0.6, 1.5, 2.5, and 3, and provided a comprehensive picture of redox compensation for $Li_2TiS_{2.4}Se_{0.6}$, the member of the series with the highest gravimetric capacity. Changes in the Se/S ratio in the compound induce changes in the local arrangement of the $TiCh_6$ (Ch=S, Se) octahedra. The subtle changes are associated with a seemingly enhanced overlap between Ti 3d and S 3p states, as well as increased charge transfer from Se to Ti, consistent with a picture where mixing S and Se produces compounds with Ti 3d-S 3p-Se 4p states just below the Fermi level that play a crucial role in activating the electrochemical behavior of $Li_2TiS_{3-y}Se_y$. Cycling of the Li within $Li_2TiS_{2.4}Se_{0.6}$ led to the concurrent activity of S and Se centers. The formation of formally S^{n-} and Se^{n-} (n<2) species was suggested from XAS analysis, and EXAFS analysis provided direct evidence of the formation of Se_2^{2-} units with Se-Se distances below 2.5 Å. These intricate processes are reversible, but there exists some hysteresis in the pathways followed by discharge versus charge. Our research highlights the synergistic role exhibited by S and Se in the same layered structure, even in the presence of a d^0 metal, providing precise definitions of how the covalent bonds can be manipulated to induce unique electrochemical activity in compounds with attractive earth abundance.

4. Experimental Section

Material Synthesis: The synthesis followed the procedure mentioned in the Leube *et. al.*[22]. The reagents were mixed and ground in stoichiometric ratios. Then, the mixture was calcined in an alumina crucible in an evacuated quartz tube under vacuum. For $Li_2TiS_{3-y}Se_y$ synthesis, the reaction mixture consisting of hand-ground Li_2S, Li_2Se, $TiSe_2$, and TiS_2 were heated to 973 K for 48 h, and then a cooling rate of 5 K/min was applied. For Li_2TiSe_3 the synthesis temperature was reduced to 873 K for 72 h.

X-ray powder diffraction: Powder X-ray diffraction experiment samples were performed on a Bruker D8 Advance diffractometer equipped with a Cu-Kα source (λ1= 1.54056 Å, λ2= 1.54439 Å) and a LynxEye detector. The data was collected in reflection mode in Bragg-Brentano geometry. Analysis and refinements of the as-collected diffraction patterns were carried out using the FullProf program suite.

Electrochemical characterization: The electrochemical characterization followed the procedure mentioned in Leube *et al.*[22] All galvanostatic electrochemical cycling of $Li_2TiS_{3-y}Se_y$ was performed with BioLogic potentiostats in Li half-cell configuration. The as synthesized cathode materials were thoroughly ground with 15 wt% electrically conducting carbon Super-P. Conductive carbon mixed cathode was then used to make Swagelok cell type cells with loadings of 5-10 mg of the cathode material, Whatman GF/D borosilicate glass fiber membranes as the separator, LP30 (Elyte, 1 M $LiPF_6$ in 1/1 wt/wt DMC/EC, 18 drops ≈ 0.2 mL) as electrolyte and a disc of metallic Li as anode were assembled in an Ar-filled glovebox. The cells were allowed to rest for 30 min and were then cycled between 3.0 V and 1.7 V at a C/10 rate, corresponding to the removal of 1 Li per formula unit.

XAS: Ti $L_{2,3}$-edge X-ray absorption spectroscopy (XAS) measurements were carried out at beamline 29-ID at Advanced Photon Source (APS) at Argonne National Laboratory (ANL). To verify the electronic environment, Ti $L_{2,3}$-edge spectra were collected in TEY and TFY modes at room temperature and under ultra-high vacuum conditions (below 10^{-8} Torr). Contributions from visible light were carefully minimized before the acquisition, and all spectra were normalized by the current from freshly evaporated gold on a fine grid positioned upstream of the main chamber. The measured spectra were aligned using beamline reference and a basic normalization using a linear background.

X-ray absorption measurements at the Se K-edge of the pristine sample and S K-edge of pristine and cycled samples were done at beamline 9-BM-B, and Se K-edge XAS measurements of the cycled samples were collected at the MRCAT beamline 10-ID-B. XAS measurement at the Ti K-edge of pristine and cycled samples was measured at beamline 5-BM-D. All the beamlines are at the Advanced Photon Source, Argonne National Laboratory (ANL). X-ray absorption spectra were collected in transmission and fluorescence mode using an ion chamber and Vortex(5-BM-D)/PIPS(9-BM-B)/Ion-chamber(10-ID-B) detectors, respectively. For S K- and Ti K-edge, the sample was smeared on carbon tape and sandwiched between Kapton tape and a thin mylar sheet, with the mylar sheet facing the incident beam. For the Se K-edge measurement, the sample was smeared on scotch tape, folded, and sandwiched between Kapton tape layers. All sample preparations were done in an Argon glovebox. The incident beam was monochromatized by using a Si (111) fixed-exit, double-crystal monochromator. For calibration at the Se K-edge, Se metal reference foil was measured simultaneously with each sample for energy calibration. Ti foil and sodium thiosulfate were used to calibrate Ti K-edge and S K-edge XAS, respectively. Basic data processing and EXAFS fitting were done using the Athena and Artemis programs from the IFEFFIT DEMETER package.[52] The S K-edge XANES fitting and Se K-edge wavelet transforms[53] were performed using the Larch XAFS package.[54] The pre-edge feature of the S K-edge was fitted with pseudo-Voigt functions, and the edge was fitted with a Gaussian function.[46,55] Se K-edge wavelet transforms were performed with continuous Cauchy mother wavelet by using the plugin available in Larch.[54,56]

Supporting Information

Supporting Information is available from the Wiley Online Library or from the author.

Acknowledgments

This work was supported by the National Science Foundation *via* grant DMR-2118020. Research conducted at beamlines 5-BM-D, 9-BM-B, 10-ID-B, and 29-ID used resources of the Advanced Photon Source, an Office of Science User Facility operated for the U.S. Department of Energy (DOE) Office of Science by Argonne National Laboratory under Contract No. DE-AC02-06CH11357. Authors sincerely thank Dr. Bruce Ravel and Dr. John Freeland for having a discussion on the data. Authors also want to thank Prof. Kimberley See for her insightful seminar at UIC.

Conflict of Interest

The authors declare no conflict of interest.

Keywords: Anionic Redox• Lithium-ion battery • X-ray absorption spectroscopy • EXAFS • coordination environments

Data Availability Statement

The data that support the findings of this study are available from the corresponding author upon reasonable request.

References

[1] M. Li, J. Lu, Z. Chen, K. Amine, *Adv. Mater.* **2018**, *30*, 1800561.
[2] J. Xu, X. Cai, S. Cai, Y. Shao, C. Hu, S. Lu, S. Ding, *Energy Environ. Mater.* **2023**, *6*, e12450.
[3] T. Chen, Y. Jin, H. Lv, A. Yang, M. Liu, B. Chen, Y. Xie, Q. Chen, *Trans. Tianjin Univ.* **2020**, *26*, 208.
[4] N. Nitta, F. Wu, J. T. Lee, G. Yushin, *Mater. Today* **2015**, *18*, 252.
[5] S. Zhao, Z. Guo, K. Yan, S. Wan, F. He, B. Sun, G. Wang, *Energy Storage Mater.* **2021**, *34*, 716.
[6] D. Weber, Đ. Tripković, K. Kretschmer, M. Bianchini, T. Brezesinski, *Eur. J. Inorg. Chem.* **2020**, *2020*, 3117.
[7] H. Li, A. J. Perez, B. Taudul, T. D. Boyko, J. W. Freeland, M.-L. Doublet, J.-M. Tarascon, J. Cabana, *ACS Energy Lett.* **2021**, *6*, 140.
[8] B. Li, D. Xia, *Adv. Mater.* **2017**, *29*, 1701054.
[9] M. Li, T. Liu, X. Bi, Z. Chen, K. Amine, C. Zhong, J. Lu, *Chem. Soc. Rev.* **2020**, *49*, 1688.
[10] J. J. Zak, S. S. Kim, F. A. L. Laskowski, K. A. See, *J. Am. Chem. Soc.* **2022**, *144*, 10119.
[11] D.-H. Seo, J. Lee, A. Urban, R. Malik, S. Kang, G. Ceder, *Nat. Chem.* **2016**, *8*, 692.
[12] M. Ben Yahia, J. Vergnet, M. Saubanère, M.-L. Doublet, *Nat. Mater.* **2019**, *18*, 496.
[13] G. Assat, D. Foix, C. Delacourt, A. Iadecola, R. Dedryvère, J.-M. Tarascon, *Nat. Commun.* **2017**, *8*, 2219.
[14] F. Flamary-Mespoulie, A. Boulineau, H. Martinez, M. R. Suchomel, C. Delmas, B. Pecquenard, F. Le Cras, *Energy Storage Materials* **2020**, *26*, 213.
[15] S. Saha, G. Assat, M. T. Sougrati, D. Foix, H. Li, J. Vergnet, S. Turi, Y. Ha, W. Yang, J. Cabana, G. Rousse, A. M. Abakumov, J.-M. Tarascon, *Nat. Energy* **2019**, *4*, 977.
[16] C. F. van Bruggen, R. J. Haange, G. A. Wiegers, D. K. G. de Boer, *Physica* **1980**, *99*, 166.
[17] J. Rouxel, *Chem. Eur. J.* **1996**, *2*, 1053.
[18] E. Nowack, D. Schwarzenbach, T. Hahn, *Acta Crystallogr. B* **1991**, *47*, 650.
[19] S. Nehzati, N. V. Dolgova, D. Sokaras, T. Kroll, J. J. H. Cotelesage, I. J. Pickering, G. N. George, *Inorg. Chem.* **2018**, *57*, 10867.
[20] M. E. Fleet, S. L. Harmer, X. Liu, H. W. Nesbitt, *Surf. Sci.* **2005**, *584*, 133.
[21] B. Li, N. Jiang, W. Huang, H. Yan, Y. Zuo, D. Xia, In *Studies on Anionic Redox in Li-Rich Cathode Materials of Li-Ion Batteries* (Ed.: Li, B.), Springer, Singapore, **2019**, pp. 99–121.

[22] B. T. Leube, C. Robert, D. Foix, B. Porcheron, R. Dedryvère, G. Rousse, E. Salager, P.-E. Cabelguen, A. M. Abakumov, H. Vezin, M.-L. Doublet, J.-M. Tarascon, *Nat. Commun.* **2021**, *12*, 5485.
[23] A. J. Martinolich, J. J. Zak, D. N. Agyeman-Budu, S. S. Kim, N. H. Bashian, A. Irshad, S. R. Narayan, B. C. Melot, J. Nelson Weker, K. A. See, *Chem. Mater.* **2021**, *33*, 378.
[24] X. Xue, X. Song, W. Yan, M. Jiang, F. Li, X. L. Zhang, Z. Tie, Z. Jin, *ACS Appl. Mater. Interfaces* **2022**, *14*, 48734.
[25] H.-J. Noh, J.-S. Kang, S. S. Lee, G. Kim, S.-W. Han, S.-J. Oh, J.-Y. Kim, H.-G. Lee, S. Yeo, S. Guha, S.-W. Cheong, *EPL* **2007**, *78*, 27004.
[26] F. Farges, G. E. Brown, J. J. Rehr, *Phys. Rev. B* **1997**, *56*, 1809.
[27] L. Zhang, D. Sun, J. Kang, H.-T. Wang, S.-H. Hsieh, W.-F. Pong, H. A. Bechtel, J. Feng, L.-W. Wang, E. J. Cairns, J. Guo, *Nano Lett.* **2018**, *18*, 4506.
[28] F. M. F. de Groot, M. O. Figueiredo, M. J. Basto, M. Abbate, H. Petersen, J. C. Fuggle, *Phys Chem Minerals* **1992**, *19*, 140.
[29] G. S. Henderson, X. Liu, M. E. Fleet, *Phys Chem Min* **2002**, *29*, 32.
[30] P. Krüger, *Phys. Rev. B* **2010**, *81*, 125121.
[31] L. Lätsch, S. A. Guda, V. Romankov, C. Wartmann, J.-M. Neudörfl, J. Dreiser, A. Berkessel, A. A. Guda, C. Copéret, *J. Am. Chem. Soc.* **2024**, *146*, 7456.
[32] J. P. Crocombette, F. Jollet, *J. Phys. Condens. Matter* **1994**, *6*, 10811.
[33] Y. Hwu, Y. D. Yao, N. F. Cheng, C. Y. Tung, H. M. Lin, *Nanostructured Materials* **1997**, *9*, 355.
[34] J. Zaanen, G. A. Sawatzky, J. Fink, W. Speier, J. C. Fuggle, *Phys. Rev. B* **1985**, *32*, 4905.
[35] F. M. F. de Groot, J. C. Fuggle, B. T. Thole, G. A. Sawatzky, *Phys. Rev. B* **1990**, *41*, 928.
[36] C. Branci, M. Womes, P. E. Lippens, J. Olivier-Fourcade, J. C. Jumas, *J. Solid State Chem.* **2000**, *150*, 363.
[37] C.-H. Lin, M. Topsakal, K. Sun, J. Bai, C. Zhao, E. Dooryhee, P. Northrup, H. Gan, D. Lu, E. Stavitski, Y. K. Chen-Wiegart, *J. Mater. Chem. A* **2020**, *8*, 12339.
[38] Z. Y. Wu, F. Lemoigno, P. Gressier, G. Ouvrard, P. Moreau, J. Rouxel, C. R. Natoli, *Phys. Rev. B* **1996**, *54*, R11009.
[39] R. Hoffmann, *Angew. Chem. Int. Ed. Engl.* **1987**, *26*, 846.
[40] J. T. Henthorn, R. J. Arias, S. Koroidov, T. Kroll, D. Sokaras, U. Bergmann, D. C. Rees, S. DeBeer, *J. Am. Chem. Soc.* **2019**, *141*, 13676.
[41] J. Timoshenko, A. Kuzmin, *Comput. Phys. Commun.* **2009**, *180*, 920.
[42] B. Li, K. Kumar, I. Roy, A. V. Morozov, O. V. Emelyanova, L. Zhang, T. Koç, S. Belin, J. Cabana, R. Dedryvère, A. M. Abakumov, J.-M. Tarascon, *Nat. Mater.* **2022**, *21*, 1165.
[43] X. Chen, L. Liu, Z. Liu, M. A. Marcus, W.-C. Wang, N. A. Oyler, M. E. Grass, B. Mao, P.-A. Glans, P. Y. Yu, J. Guo, S. S. Mao, *Sci. Rep.* **2013**, *3*, 1510.
[44] C. J. Hansen, J. J. Zak, A. J. Martinolich, J. S. Ko, N. H. Bashian, F. Kaboudvand, A. Van der Ven, B. C. Melot, J. Nelson Weker, K. A. See, *J. Am. Chem. Soc.* **2020**, *142*, 6737.
[45] G. Sun, Z. Wei, N. Chen, G. Chen, C. Wang, F. Du, *Chem. Eng. J.* **2020**, *388*, 124305.
[46] K. Rose, S. E. Shadle, M. K. Eidsness, D. M. Kurtz, R. A. Scott, B. Hedman, K. O. Hodgson, E. I. Solomon, *J. Am. Chem. Soc.* **1998**, *120*, 10743.
[47] A. Jentys, *Phys. Chem. Chem. Phys* **1999**, *1*, 4059.
[48] B. S. Clausena, H. Topsøe, L. B. Hansen, P. Stoltze, J. K. Nørskov, *Catal. Today* **1994**, *21*, 49.
[49] R. Hoffmann, S. Shaik, J. C. Scott, M.-H. Whangbo, M. J. Foshee, *Journal of Solid State Chemistry* **1980**, *34*, 263.
[50] B. J. Bellott, R. G. Haire, J. A. Ibers, *Zeitschrift für anorganische und allgemeine Chemie* **2012**, *638*, 1777.
[51] S. J. Hibble, D. A. Rice, D. M. Pickup, M. P. Beer, *J. Chem. Soc., Faraday Trans.* **1996**, *92*, 2131.
[52] B. Ravel, M. Newville, *J. Synchrotron Radiat.* **2005**, *12*, 537.
[53] M. Muñoz, P. Argoul, F. Farges, *Am. Mineral.* **2003**, *88*, 694.
[54] M. Newville, *J. Phys.: Conf. Ser.* **2013**, *430*, 012007.

[55] A. L. Tenderholt, R. K. Szilagyi, R. H. Holm, K. O. Hodgson, B. Hedman, E. I. Solomon, *Inorg. Chem.* **2008**, *47*, 6382.
[56] M. Newville, *13.6. XAFS: Wavelet Transforms for XAFS — xraylarch 0.9.74 documentation*, **2024**.